symmetry

MDPI

Article

Reliability Analysis of the Freeze–Thaw Cycle of Aeolian Sand Concrete Based on a Dual Neural Network in Series Structure Failure Mode

Yun He [1,*], Huijun Xue [1,*] and Juan Du [2]

[1] College of Water Conservancy and Civil Engineering, Inner Mongolia Agricultural University, Hohhot 010018, China
[2] College of Statistics and Mathematics, Inner Mongolia University of Finance and Economics, Hohhot 010070, China; djsd2007@126.com
* Correspondence: heyun1021@163.com (Y.H.); xuehuijun@yeah.net (H.X.); Tel.: +86-15774715939 (Y.H.); +86-18698406289 (H.X.)

Abstract: Aeolian sand is a low-quality natural resource widely distributed in Inner Mongolia, China. Aeolian sand concrete has been developed as a primary raw material and tested to determine its frost resistance durability. In this study, the mechanism of concrete durability damage and deterioration was determined through the use of relative dynamic elastic modulus and mass loss ratio macroscopic evaluation indices, scanning electron microscopy (SEM), and X-ray diffraction (XRD). According to the mathematical statistics method, the marginal statistical distribution of each damage parameter was obtained, and the Copula method of series structural failure mode was proposed to construct the joint probability density function of concrete structural damage parameters. Structural reliability was analyzed via the dual neural network method, and the reliability of aeolian sand concrete was calculated in order to accurately predict the number of freeze–thaw cycles involved in structural failure. The findings of the present study indicate that the relative dynamic elastic modulus decreases progressively while mass loss increases gradually during an increasing number of freeze–thaw cycles. This result effectively illustrates the degradation pattern of the aeolian sand concrete specimens' frost resistance. The reliability analysis model developed in the present study can effectively capture the correlation between structural reliability and freeze–thaw cycles in concrete structures, enabling accurate prediction of the remaining lifespan of aeolian sand concrete.

Keywords: aeolian sand concrete; freeze–thaw cycle; dual neural network; dynamic elastic modulus; mass loss rate

Citation: He, Y.; Xue, H.; Du, J. Reliability Analysis of the Freeze–Thaw Cycle of Aeolian Sand Concrete Based on a Dual Neural Network in Series Structure Failure Mode. *Symmetry* **2024**, *16*, 782. https://doi.org/10.3390/sym16070782

Academic Editors: Zine El Abiddine Fellah and Sergei D. Odintsov

Received: 28 April 2024
Revised: 27 May 2024
Accepted: 18 June 2024
Published: 21 June 2024

1. Introduction

Aeolian sand is a widely used material in engineering that can be used as a fine aggregate to prepare concrete to ensure that it meets the requirements of general engineering applications [1]. Research status of aeolian sand concrete has been studied and applied as engineering material for a long time, and many scholars regarded aeolian sand as fine aggregate. The use of aeolian sand to replace all or part of river sand in the preparation of concrete had a certain scope and application prospect in the area where river sand resources are scarce [2]. As for the workability of aeolian sand concrete, the research shows that the partial replacement of river sand by aeolian sand can improve the workability of concrete [3,4]. Both the collapse and water absorption of concrete increased with the increase in the aeolian sand replacement rate [5]. For the mechanical properties of aeolian sand concrete, the research shows that the strength of aeolian sand concrete was inversely proportional to amount of aeolian sand [6]. The mechanical properties of aeolian sand concrete can be improved effectively by using fiber, chemical admixtures and mineral admixtures [7,8]. As for the frost resistance of aeolian sand concrete, the research shows

that aeolian sand within 30% can effectively inhibit the freeze–thaw damage of light aggregate concrete [9]. The introduction of aeolian sand can affect the spatial arrangement of hydration products [10].

Regarding the chosen concrete reliability analysis method, a considerable amount of research has been carried out by domestic and international scholars. Zhao Gaosheng et al. used the finite volume method and the Monte Carlo simulation method to study the reliability of marine concrete with different sections of the material being subjected to chloride ion corrosion. The results of this study demonstrate that the finite volume method yields high accuracy in reliability analysis and highlights the significant impact of section shape on the durability of concrete structures [11]. Jiang et al. proposed a specific reliability evaluation method based on multiple degradation factors. The copula function was applied to combine two edge distribution functions in order to derive the joint distribution function, and the residual durability reliability model was subsequently established. The validity of the model was later verified using experimental data [12]. Lydia et al. established a mechanical reliability model of reliability index and failure probability for square composite columns filled with ordinary concrete and high-performance concrete under axial compression by using the response surface method. The findings of their study indicate that the properties and dimensions of the column play a crucial role in determining its strength and reliability. This approach was applied to assess the responsiveness of random parameters in terms of structural reliability [13]. Qiao Hongxia et al. established a freeze–thaw failure reliability calculation model based on Palmgren's theory to predict the remaining life of ceramic powder reclaimed concrete. The reliability calculation model of freeze–thaw failure based on the Palmgren model has been proven to be highly reliable through calculation and verification. The model accurately depicts the correlation between the reliability of ceramic powder recycled concrete and freeze–thaw cycles, making it a practical and applicable tool in various scenarios [14]. The concrete life analysis of probability theory can be divided into two categories: (1) the reliability function of concrete can be established by using the Wiener distribution probability method to reflect the remaining life of specimens with the optimal ratio [15,16], and (2), based on the Weibull probability method, a failure model can be established with concrete mass loss and relative dynamic elastic modulus as indexes for freeze–thaw reliability analysis [17,18]. According to the latest domestic and international research findings in this field, a significant portion of studies are primarily focused on qualitative research. The utilized analysis methodology predominantly delineates the degradation patterns through experimental data, with minimal utilization of artificial intelligence models for advanced life prediction and reliability analysis. Simultaneously, the traditional approaches exhibit certain limitations in that they rely exclusively on linear regression, making it challenging to ensure precise fitting accuracy for reliability models characterized by strong nonlinearity.

A neural network can accurately fit nonlinear functions; as a result, it possesses a multitude of applications in material constitutive relations and parameter fitting. Gasperlin M. et al. proposed the basic mathematical model of a neural network to predict the viscoelastic behavior of an emulsion system with a certain degree of accuracy [19]. Xue J. et al. introduced a highly effective approach leveraging artificial neural networks. Taking typical concrete materials as an example, the authors established a macroscopic analytical strength criterion from three steps of the nonlinear homogenization process. This model can effectively predict the friction coefficient and cohesion of porous cement slurry on a microscopic scale with good accuracy [20]. Al-Haik M. S. et al. studied the stress–relaxation behavior of polymer composites based on artificial neural networks and predicted a broader range of nonlinear models more accurately [21]. Logsig function and Tansig function are commonly used as activation functions of neurons in traditional neural networks. As general function approximators, they have the following disadvantages: the calculation process of the neural network is separated from the fitting equation, which leads to poor generalization ability and low accuracy of the fitting calculation [22].

Based on the recent results of domestic and international research, most studies remain in the qualitative research stage, and the analysis method utilized primarily describes the performance degradation law with experimental data [23]. When probability theory is used for analysis, life prediction and reliability are usually analyzed via linear regression. Because the correlation between damage parameters cannot be accurately described and the failure surface is highly nonlinear, the accuracy and efficiency of reliability analysis are not high. In the present study, aeolian sand with low-quality natural resources was used as concrete fine aggregate. Firstly, we carried out a frost resistance durability test on the aeolian sand concrete, and the microstructural characterization of the concrete was used to determine the durability damage and deterioration mechanism of the concrete through the use of scanning electron microscopy (SEM) and X-ray diffraction (XRD). Secondly, the joint probability density function of damage parameters was constructed using a statistical method and the Copula function to accurately describe the correlation between damage parameters. Finally, due to the highly nonlinear failure surface, the dual neural network method was used to calculate the reliability and failure probability of wind-accumulated sand concrete under different mix ratios, and the reliability function was established to describe the relationship between the reliability of concrete and the freeze–thaw cycle. This method was used to reflect the concrete's remaining life, providing theoretical guidance for engineering practice and relevant evaluation and identification.

2. Test Process and Scheme Design

In the present study, we considered the design requirements of hydraulic concrete in cold areas in northwestern China. The study involved the use of replacement rates of 20%, 40% and 60% of aeolian sand to substitute natural river sand. Egg gravel and light pumice stone were taken as coarse aggregates. An air-entraining agent was added to improve the frost resistance of the concrete for use in concrete test blocks. Six groups of concrete test designs were combined, as shown in Table 1, where OC represents ordinary concrete and LAC represents lightweight aggregate concrete.

Table 1. Mixture ratios of aeolian sand concrete samples.

Group	OC–20%	OC–40%	OC–60%	LAC–20%	LAC–40%	LAC–60%
Cement/kg·m^{-3}	320	320	320	320	320	320
Fly ash/kg·m^{-3}	80	80	80	80	80	80
River sand/kg·m^{-3}	600	450	300	600	450	300
Aeolian sand/kg·m^{-3}	150	300	450	150	300	450
Crushed stone/kg·m^{-3}	1060	1060	1060	/	/	/
Pumice stone/kg·m^{-3}	/	/	/	700	700	700
Water/kg·m^{-3}	180	180	180	180	180	180
Admixture/kg·m^{-3}	6.80	6.80	6.80	6.80	6.80	6.80

The compressive strength of concrete was initially assessed under various mix ratios following the guidelines outlined in the Standard Test Method for Mechanical Properties of Ordinary Concrete (GB/T 50081-2019) [24] as indicated in Figure 1.

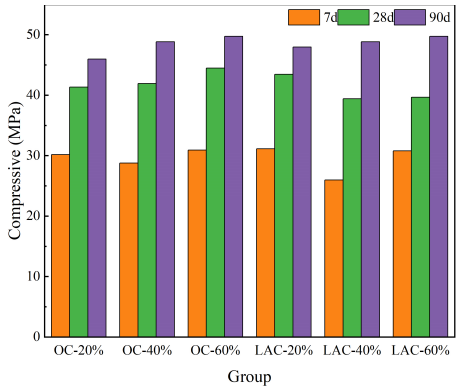

Figure 1. The compressive strength of eolian sand concrete.

3. Durability Test Results and Analysis

3.1. Failure Analysis Based on Dynamic Elastic Modulus and Mass

The relative dynamic elastic modulus and mass loss rate indicate the extent of failure in aeolian sand concrete after being subjected to a freeze–thaw cycle. The dynamic elastic modulus relative to the initial value was measured after every 25 freeze–thaw cycles.

$$P_{ij} = \frac{E_{ij}}{E_{i0}} \times 100\% \quad (1)$$

where E_{ij} is the dynamic elastic modulus of specimens in Group i after $25j$ freeze–thaw cycles; E_{i0} is the dynamic elastic modulus of specimens in Group i at the beginning of the cycle; and P_{ij} is the relative dynamic elastic modulus, $i = 1 \ldots 6$, $j = 1 \ldots 8$.

The mass loss rate of aeolian sand concrete specimen after every 25 freeze–thaw cycles is

$$W_{ij} = \frac{M_{i0} - M_{ij}}{M_{i0}} \times 100\% \quad (2)$$

where M_{ij} is the mass of group i specimens after $25j$ freeze–thaw cycles; M_{i0} is the mass of Group i specimens at the beginning of the cycle; and W_{ij} is the mass loss rate, $i = 1 \ldots 6$, $j = 1 \ldots 8$.

The relative dynamic elastic modulus of both types of aeolian sand concrete decreases as the number of freeze–thaw cycles increases, with OC–20% and OC–60% exhibiting significant attenuation, as depicted in Figure 2. After 200 freeze–thaw cycles, this attenuation reaches more than 60%; in contrast, LAC–20% and LAC–40% attenuated less than 5%. Based on the relative dynamic elastic modulus index, aeolian sand lightweight aggregate concrete exhibits superior frost resistance compared to ordinary concrete containing aeolian sand.

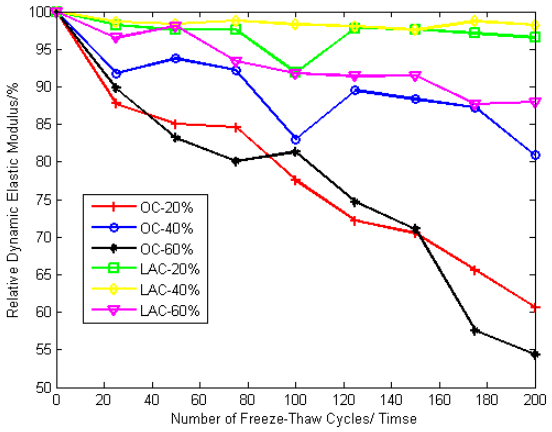

Figure 2. Relative dynamic modulus changes with the number of freeze–thaw cycles.

The quality loss rate of the two types of zeolite sand concrete was found to increase with an increase in the number of freeze–thaw cycles, as depicted in Figure 3. OC–60% and LAC–60% showed a significant mass loss, and after 200 freeze–thaw cycles, their loss rate was found to be more than 5%; in comparison, the mass loss rate of the other four types of concrete was relatively low. Concrete with aeolian sand replacement rates of 20% and 40% showed better freeze–thaw failure resistance than concrete with a 60% replacement rate.

With the increasing number of freeze–thaw cycles, the damage to the surface and internal structure of eolian sand concrete is aggravated. These results are in accordance with the relevant requirements of the Test Method for Long–term Performance and Durability of Ordinary Concrete (GB/T 50082-2009) [25]. In the process of the freeze–thaw cycle, when the mass loss rate of concrete exceeds 5% or the relative dynamic elastic modulus decays to less than 60%, it is considered that concrete has reached the normal service limit state, that is, it has reached the damage state.

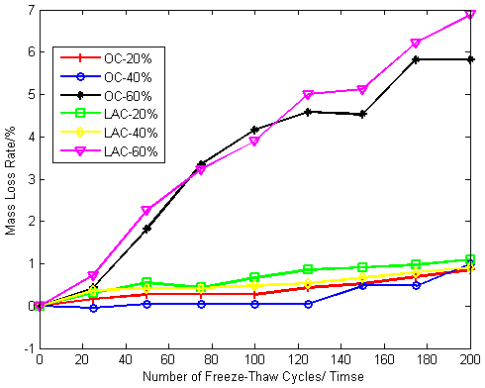

Figure 3. Mass loss rate changes with the number of freeze–thaw cycles.

3.2. Scanning Electron Microscope (SEM) Microstructure

Through the use of field–emission scanning electron microscopy (SEM) magnified 500 times [26], the macro frost resistance of the concrete was determined at the microstructural level, and the microstructural morphology of the aeolian sand concrete interface transition zone with different mix ratios before and after the freeze–thaw cycle was observed, as shown in Figures 4 and 5.

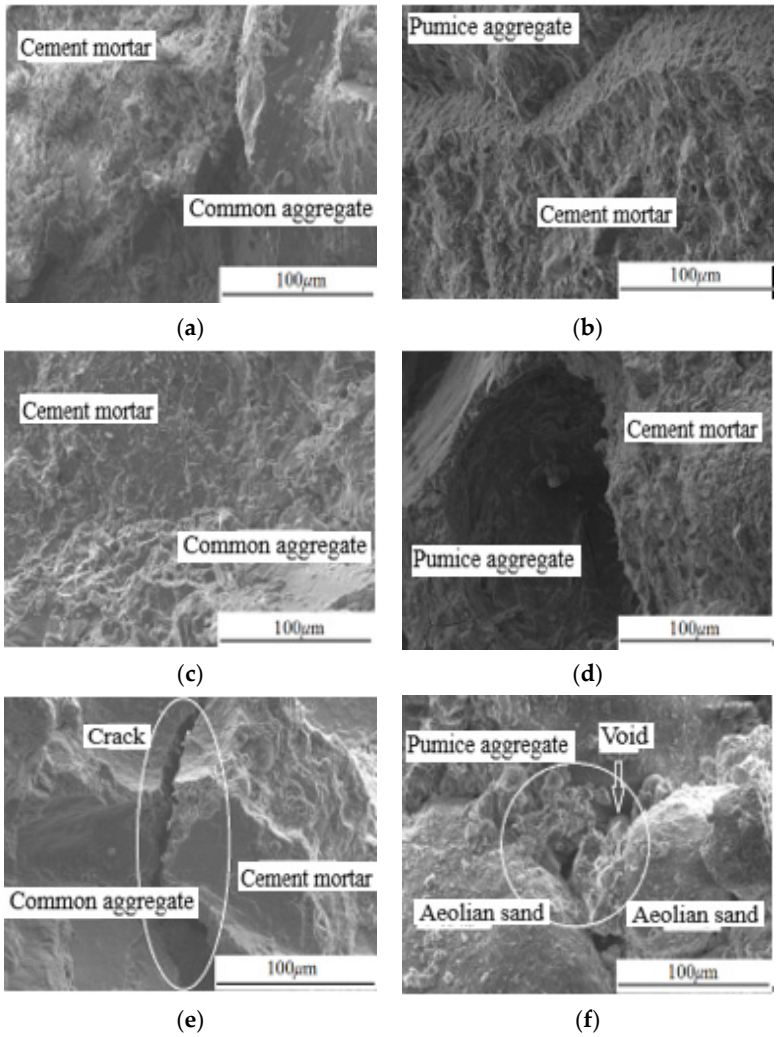

Figure 4. SEM microstructure diagram of eolian sand concrete with different mix ratios before the freeze–thaw cycle (×500). (**a**) No. 1 group (OC–20%); (**b**) No. 4 group (LAC–20%); (**c**) No. 2 group (OC–40%); (**d**) No. 5 group (LAC–40%); (**e**) No. 3 group (OC–60%); (**f**) No. 6 group (LAC–60%).

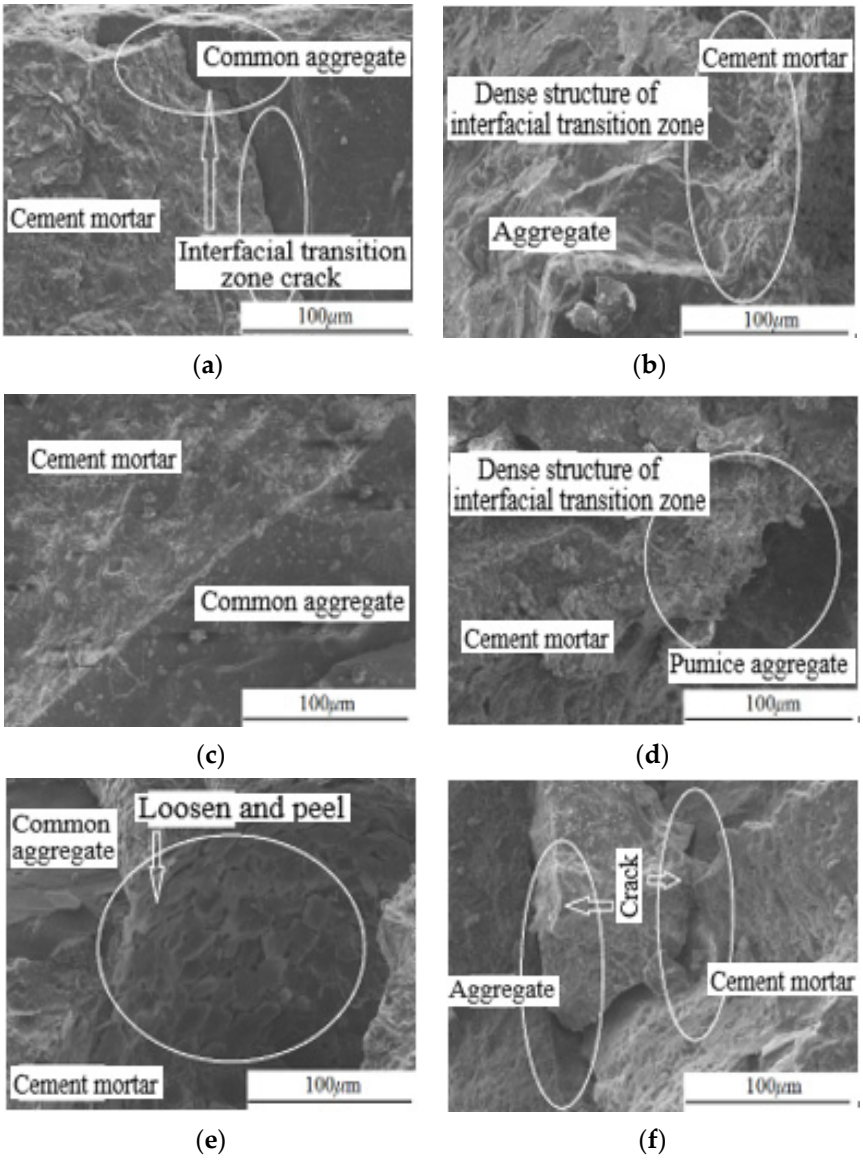

Figure 5. SEM microstructure diagram of eolian sand concrete with different mix ratios after the freeze–thaw cycle (×500). (**a**) No. 1 group (OC–20%); (**b**) No. 4 group (LAC–20%); (**c**) No. 2 group (OC–40%); (**d**) No. 5 group (LAC–40%); (**e**) No. 3 group (OC–60%); (**f**) No. 6 group (LAC–60%).

As can be seen from Figures 3 and 4, after 200 freeze–thaw cycles, the interface transition zone between OC–20% and OC–60% aggregate and cement slurry shows obvious gaps, the two phases of cement slurry and aggregate appear to show a peeling phenomenon, and the integrity of the interface transition zone worsens. The OC–40% aggregate and cement paste interface transition zone appeared to show small micro–cracks, with no obvious cracks, and its integrity was found to be satisfactory. For the LAC–20% and LAC–40% aggregate and cement slurry interface transition zone, we found some fine cracks and pores, with the fine cracks existing independently of each other with no connectivity and penetration phenomena, and the integrity was found to be satisfactory. However, the transition zone between the interface of LAC–60% lightweight aggregate and cement slurry peeled off entirely, and the cracks' size was larger. The stable "nested" structure was disturbed, and the integrity worsened significantly.

3.3. X-ray Diffraction (XRD) Phase Analysis

In order to better determine the phase composition of the two types of aeolian sand concrete cement slurry, X-ray diffraction (XRD) was used for phase composition analysis.

Figure 6 shows the XRD phase analysis of OC–40% and LAC–40% aeolian sand concrete before and after a freeze–thaw cycle.

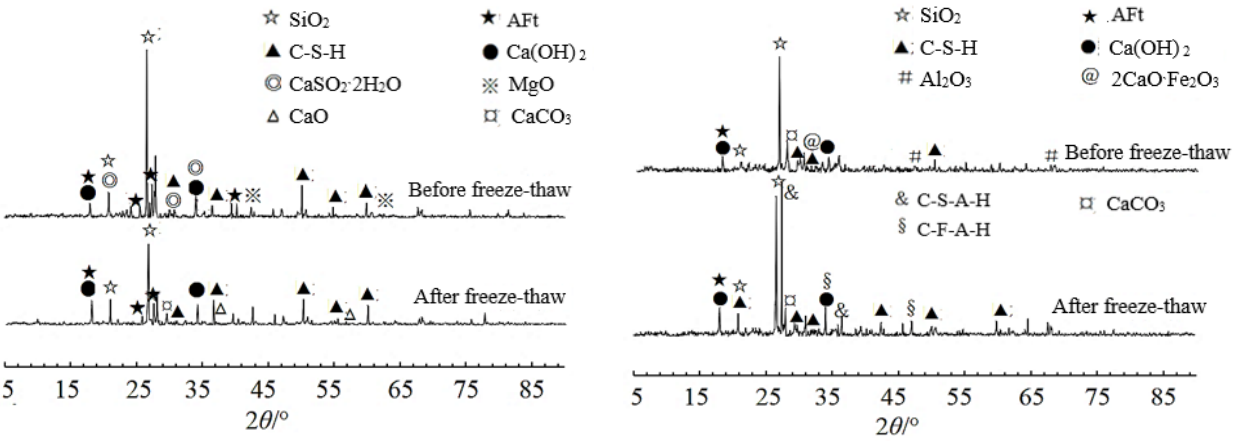

Figure 6. XRD phase analysis of cement paste in aeolian sand concrete before and after freeze–thaw cycles. (**a**) (OC–40%); (**b**) (LAC–40%).

Based on the phase analysis of aeolian sand concrete cement slurry before and after the freeze–thaw cycle, Figure 5 shows that the primary chemical constituents present are SiO_2, C–S–H gel, CH and AFt. Due to the complex hydration reaction involved in the self–setting and hardening of concrete, other components with weak diffraction peak strength have little influence on the freeze–thaw failure of concrete.

From the above analysis and comparison of microstructural morphology and phase composition, it can be seen that the physical change predominates in the freeze–thaw cycle of the two types of aeolian sand concrete; in contrast, the chemical composition of hydration products has a weak influence. The physical changes primarily result from alterations in dynamic relative elastic modulus and mass loss rate, leading to the eventual freeze–thaw failure of the concrete.

4. Construction of Aeolian Sand Concrete Damage Parameter Joint Probability Density Function

The sample size of concrete damage parameter data obtained in the experimental section of the present study is small, and the distribution law of data samples cannot be known due to many uncertain factors. Therefore, the key to accurately describing the parameter joint probability density function is determining whether reliability can be accurately calculated.

4.1. Damage Parameter Distribution Law

The statistical analysis software SPSS (version 26) was used to draw the distribution histogram of the relative dynamic elastic modulus P and mass loss rate W of OC–20% under 200 freeze–thaw cycles, as shown in Figure 7. It can be seen from the figure that the distribution of P and W is basically symmetric. Figure 8 is the P–P figure of P and W, and it can be seen that each observation point is roughly around a straight line.

In summary, the relative dynamic elastic modulus P and mass loss rate W distributions can be considered normal distributions. Thus, it is necessary to write the two–parameter edge probability density function $f_1(P)$ and $f_2(W)$ as

$$f_1(P) = \frac{1}{\sqrt{2\pi b_1^2}} \exp\left[-\frac{(x_1 - a_1)^2}{2b_1^2}\right] \tag{3}$$

$$f_2(W) = \frac{1}{\sqrt{2\pi b_2^2}} \exp\left[-\frac{(x_2 - a_2)^2}{2b_2^2}\right] \tag{4}$$

where a_1 = 60.6598 and b_1 = 7.3395; a_2 = 0.8499 and b_2 = 0.0101.

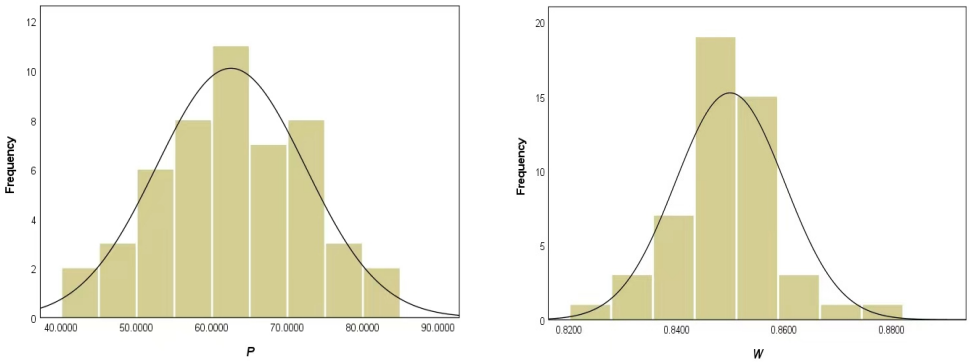

(**a**) (**b**)

Figure 7. Damage parameter histograms of OC–20% for 200 freeze–thaw cycles. (**a**) Relative dynamic elastic modulus; (**b**) Mass loss rate.

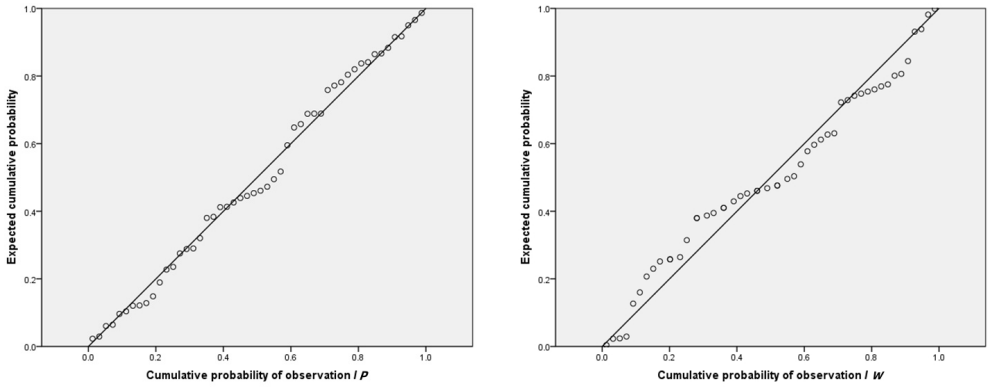

(**a**) (**b**)

Figure 8. Damage parameter P–P figure of OC–20% for 200 freeze–thaw cycles. (**a**) Relative dynamic elastic modulus; (**b**) Mass loss rate.

4.2. Copula Method for Series Structure Failure Mode

For a series structure system, a single component failure will lead to structural system failure, and then, the series system reliability P_r can be expressed as follows:

$$P_r = P(Z_1 > 0 \cap Z_2 > 0 \cap \cdots \cap Z_S > 0) = \bigcap_{s=1}^{S} Z_s > 0 \tag{5}$$

The safety domain of series system $S = \{x | \bigcap_{s=1}^{S} Z_s > 0\}$ is obtained, and the failure domain of two variables series structure failure modes is shown in Figure 9.

If we have the joint probability density function $f_X(\boldsymbol{x})$ of random variable $\boldsymbol{x} = [x_1, x_2, \ldots, x_n]^{\mathrm{T}}$, then the theoretical reliability of the series system can be determined.

$$P_r = \int_{\bigcap_{s=1}^{S} Z_s > 0} f_X(\boldsymbol{x}) \mathrm{d}\boldsymbol{x} = \int \cdots \int_{\bigcap_{s=1}^{S} Z_s > 0} f_X(x_1, x_2, \ldots, x_n) \mathrm{d}x_1 \mathrm{d}x_2 \cdots \mathrm{d}x_n \tag{6}$$

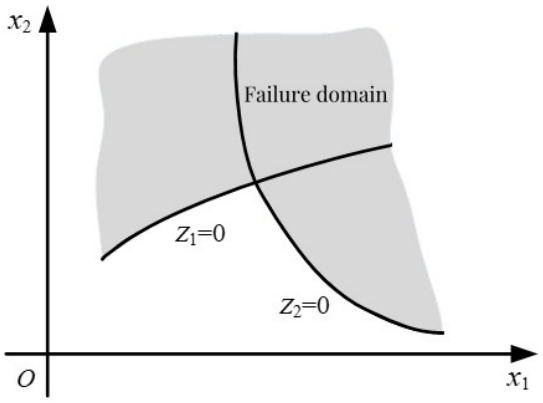

Figure 9. Failure domain of the series structure system.

As shown in Equation (6), accurately determining the joint probability density function of concrete damage parameters is crucial for determining the reliability of concrete structures. However, constructing this joint probability density function has consistently posed a significant challenge. Based on this challenge, a construction method of performance parameters' joint probability density function based on the Copula function is proposed in the present paper.

According to Sklar's theorem [27], the joint distribution function of variable $x_1, x_2, \ldots, x_n$ is expressed as $F(x_1, x_2, \cdots, x_n)$

$$F(x_1, x_2, \cdots, x_n) = C(F_1(x_1), F_2(x_2), \cdots, F_n(x_n); \theta) = C(u_1, u_2, \cdots, u_n; \theta) \tag{7}$$

where $u_i = F_i(x_i)$ is the edge distribution function of the variable X_i; $C(u_1, u_2, \cdots, u_n; \theta)$ is a Copula function; and θ is the related parameters of the Copula function.

Taking the derivative of Equation (5), the joint probability density function of variables $x_1, x_2, \ldots, x_n$ is written as $f_X(x_1, x_2, \ldots, x_n)$

$$\begin{aligned} f_X(x_1, x_2, \ldots, x_n) &= f_1(x_1) f_2(x_2) \ldots f_n(x_n) c(F_1(x_1), F_2(x_2) \ldots F_n(x_n); \theta) \\ &= c(u_1, u_2, \cdots, u_n; \theta) \prod_{i=1}^{n} f_i(x_i) \end{aligned} \tag{8}$$

where $f_i(x_i)$ is the edge probability density function of variables x_1, x_2, …, x_n and $c(u_1, u_2, \cdots, u_n; \theta) = \frac{\partial^n C(u_1, u_2, \cdots, u_n; \theta)}{\partial u_1 \partial u_2 \cdots \partial u_n}$ is the density function of the Copula function.

Table 2 shows the common Copula function types.

Table 2. Copula function types.

Copula Types	Copula Distribution Function $C(u_1, u_2, \cdots, u_n; \theta)$	θ Range of Values
Gaussian	$\varphi_n(\varphi^{-1}(u_1), \varphi^{-1}(u_2), \cdots, \varphi^{-1}(u_n); \theta)$	$[-1, 1]$
Gumbel	$\exp\left\{-\left[\sum_{i=1}^{n}(-\ln u_i)^{\theta}\right]^{\frac{1}{\theta}}\right\}$	$[1, \infty)$
Clayton	$\left(\sum_{i=1}^{n} {u_i}^{-\theta} - n + 1\right)^{-\frac{1}{\theta}}$	$(0, \infty)$
Frank	$-\frac{1}{\theta}\ln\left[1 + \frac{\prod_{i=1}^{n}(e^{-\theta u_i} - 1)}{(e^{-\theta} - 1)^{n-1}}\right]$	$n = 2, \theta \in (-\infty, \infty) \cap (\theta \neq 0)$ $n \geq 3, \theta \in (0, \infty)$

Table 2. *Cont.*

Copula Types	Copula Distribution Function $C(u_1, u_2, \cdots, u_n; \theta)$	θ Range of Values
No. 16	$\frac{1}{2}\left(A+\sqrt{A^2+4\theta}\right)$ $A=\sum_{i=1}^{n} u_i - n + 1 - \theta\left(\sum_{i=1}^{n}\frac{1}{u_i} - n + 1\right)$	$n=2, \theta \in [0,\infty)$ $n \geq 3, \theta \in (0.1863,\infty)$
Plackett	$\frac{B-\sqrt{B^2-4u_1u_2\theta(\theta-1)}}{2(\theta-1)}$ $B=1+(\theta-1)(u_1-u_2)$	$(0,\infty)\backslash\{1\}$

4.3. Construction of Concrete Structures Damage Parameter Joint Probability Density Function

The joint probability density function $f_X(P,W)$ construction of the relative dynamic elastic modulus P and mass loss rate W under 200 freeze–thaw cycles of OC–20% is taken as an example to illustrate the method.

We first drew the test scatter plot for P and W, with the black dots shown in Figure 10. As can be seen from the figure, there is a positive correlation between the two parameters; therefore, the function that can express the positive correlation was selected as the Copula function. To construct a two–parameter joint probability density function, relevant parameter values of each Copula function were obtained, as shown in Table 3.

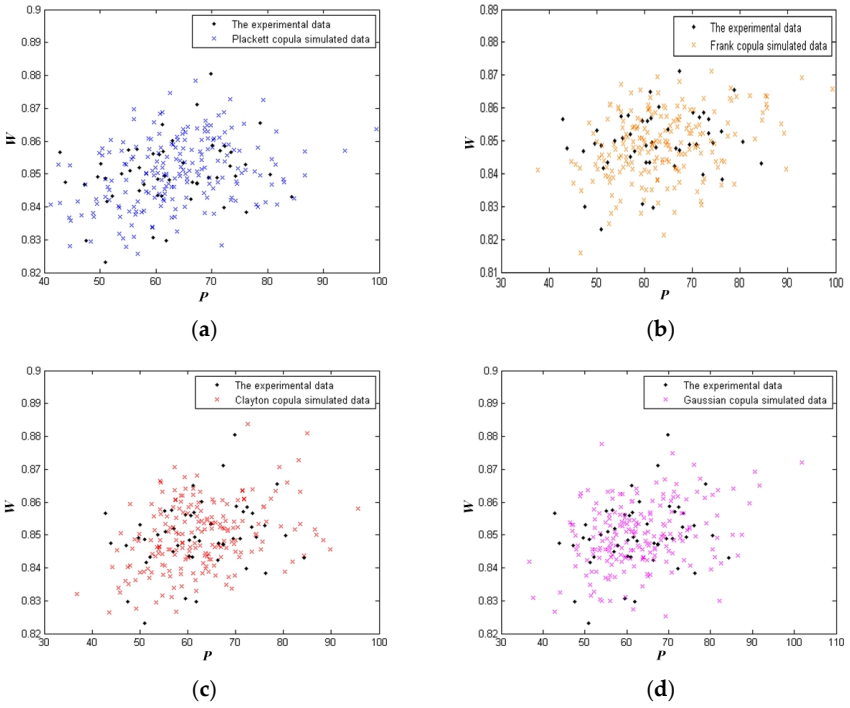

Figure 10. Scatter plots of simulated variables for different copula functions. (**a**) Plackett Copula; (**b**) Frank Copula; (**c**) Clayton Copula; (**d**) Gaussian Copula.

Table 3. θ value of related parameters for each Copula function.

Copula Function	Gaussian	Plackett	Frank	Clayton
θ value	0.33	2.97	2.25	0.59

Figure 10 shows the scatter plots simulated by each Copula function when the number of simulations n = 200. It can be seen from the figure that the scatter plot generated by each Copula function can suitably cover the original observed data of relative dynamic elastic

modulus and mass loss rate, demonstrating the ability of the Copula function to fit the measured data.

The joint probability density function $f_X(P, W)$ of relative dynamic elastic modulus P and mass loss rate W can be written as:

$$f_X(P, W) = f_1(P) f_2(W) c(f_1(P), f_2(W); \theta) \tag{9}$$

5. Analysis of Reliability Results Based on the Dual Neural Network

Considering that the performance function of the concrete structure is Z = G(P,W), the joint probability distribution function of basic random variable X = (P,W) is F_X(P,W), and the joint probability density function is f_X(P,W), then the reliable probability P_r of the concrete structure can be written as follows:

$$\begin{aligned} P_r &= \int\limits_{Z>0} dF_X(P, W) = \int\limits_{Z>0} f_X(P, W) dX \\ &= \int \cdots \int_{Z>0} f_X(P, W) dP dW \end{aligned} \tag{10}$$

It is widely known that a concrete structural system consists of two series of performance function components. According to the Standard Test Method for Long–Term Performance and Durability of Ordinary Concrete (GB/T 50082-2009), once the relative dynamic elastic modulus reaches 60% or the mass loss rate reaches 5%, the concrete specimen meets the failure criteria. Its performance function expression is shown in Equation (11):

$$\begin{cases} G_1(P) = P - 60\% \\ G_2(W) = 5\% - W \end{cases} \tag{11}$$

5.1. Dual Neural Network Method

The reliability of a concrete structure can be calculated based on the defined series structural reliability.

$$P_r = \int_{\mu_W - 4\delta_W}^{\mu_W + 4\delta_W} \int_{\mu_P - 4\delta_P}^{\mu_P + 4\delta_P} I(G_1(P), G_2(W), P, W) \cdot f_X(P, W) \mathrm{d}P \mathrm{d}W \tag{12}$$

where the indicated function $I(G_1(P), G_2(W), P, W)$ takes on 1 when min $(G_1(P), G_2(W)) > 0$; otherwise, it is equal to 0.

It can be observed that neural network A, which comprises three layers, can represent the original function of multiple integrals, as stated by a multi–layer neural network capable of approximating any nonlinear function with high precision. The network structure is shown in Figure 11. The input and output relation in scalar form is:

$$Y^* = \sum_{j=1}^{m} w_j f(\sum_{i=1}^{n} k_{ji} x_i + b_j) + c \tag{13}$$

It can be respectively determined via the partial derivation of variables $x_1, x_2, \cdots, x_n$

$$y^* = \frac{\partial^n Y}{\partial x_1 \partial x_2 \cdots \partial x_n} = \sum_{j=1}^{m} k_{j1} k_{j2} \cdots k_{jn} w_j f^{(n)}(\sum_{i=1}^{n} k_{ji} x_i + b_j) \tag{14}$$

If $W_j = k_{j1} k_{j2} \cdots k_{jn} w_j$, Equation (14) can be written as a function of network output and input variables:

$$y^* = \sum_{j=1}^{m} W_j f^{(n)}(\sum_{i=1}^{n} k_{ji} x_i + b_j) \tag{15}$$

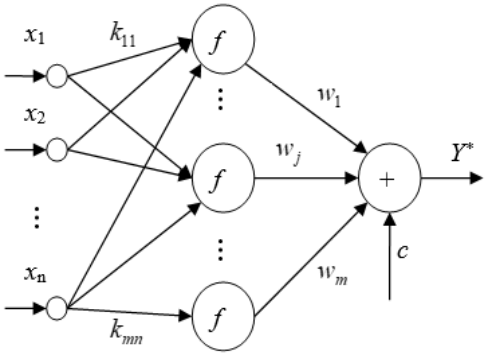

Figure 11. Original function network A structure.

If $f = e^x$, Equation (15) can be simplified as

$$y^* = \sum_{j=1}^{m} W_j f(\sum_{i=1}^{n} k_{ji} x_i + b_j) \tag{16}$$

The neural network B structure is illustrated in Figure 12.

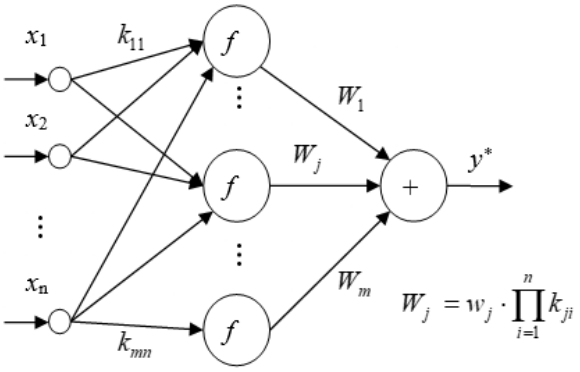

Figure 12. Integrand network B structure.

Evidentially, the original function of integrand y^* in Equation (16) is Y^*. Therefore, neural network A and neural network B are considered dual neural networks [28].

By comparing Equations (13) and (16), it can be seen that the original function network and integrand function network have the same network structure and are both three–layer neural networks with n input, single output, and m hidden layer elements. The above two networks are related in connection weight, threshold, and activation function type. In the integrated function network B, the connection weight from the input layer to the hidden layer element is k_{ji}, the connection weight from the hidden layer to the output layer element is W_j. Original function network A the connection weight from the input layer to the hidden layer unit is k_{ji}, the connection weight of the hidden layer to the output layer unit is $W_j / \prod_{i=1}^{n} k_{ji}$, the threshold value of the output layer unit is c. Based on the above structure, it can be observed that when network B in a dual neural network satisfies the given relation and approximates the integrand function in the integral, network A approximates the original function.

It can be seen from the theory of multivariate integration that the integral value can be expressed as the weighted algebraic sum of the original function Y^* at the hypercube vertices $D^* = \{(x_1, x_2, \cdots, x_n) | x_1^1 \le x_1 \le x_1^2, x_2^1 \le x_2 \le x_2^2, \cdots, x_n^1 \le x_n \le x_n^2\}$, specifically expressed as follows:

$$J^* = \sum_{m_1=1}^{2} \sum_{m_2=1}^{2} \cdots \sum_{m_n=1}^{2} (-1)^{\sum_{k=1}^{n} m_k} Y^*(x_1^{m_1}, x_2^{m_2}, \cdots, x_n^{m_n}) \quad (17)$$

The dual neural network method was used to integrate Equation (12), and the reliability of OC–20% under 200 freeze–thaw cycles was determined.

The variables P and W are divided into equal parts in the interval 100, and the integrand function network B is crossed in pairs to form the input sample point, and the network output value of the corresponding sample point is calculated using the integrand function. The training sample is shown in Table 4.

Table 4. Training samples of network B.

W	P					
	31.3018	31.8890	32.4761	……	89.4306	90.0178
0.8095	0	0	0	……	0.0868×10^{-8}	0.0680×10^{-8}
0.8103	0	0	0	……	0.1136×10^{-8}	0.0837×10^{-8}
0.8111	0	0	0.0732×10^{-8}	……	0.1458×10^{-8}	0.1260×10^{-8}
⋮	⋮	⋮	⋮	……	……	……
0.8895	0.0898×10^{-8}	0.1286×10^{-8}	0.1766×10^{-8}	……	0.1284×10^{-8}	0.0877×10^{-8}
0.8903	0.0744×10^{-8}	0.0873×10^{-8}	0.1245×10^{-8}	……	0.0915×10^{-8}	0.0702×10^{-8}

Using the dual neural network relation, the original function network A is obtained. The vertices of the hypercube in the input sample of network B are simulated through network A, and the sample points are shown in Table 5. The numerical solution of the integral, namely the structural reliability, can be obtained by substituting the simulation values into Equation (17).

Table 5. Simulation samples of network A.

P	90.0178	90.0178	31.3018	31.3018
W	0.8903	0.8095	0.8903	0.8095

Through the above calculation, the structural reliability and failure probability of OC–40%, OC–60%, LAC–20%, LAC–40% and LAC–60% under 200 freeze–thaw cycles can be similarly obtained, as outlined in Tables 5 and 6. To further illustrate the performance of the proposed method, the Weibull probability distribution model (WPDM) was used for evaluation.

Table 6. Reliability calculation results using different methods.

	Proposed Method	**WPDM**	**MCS**
OC–20%	0.977767	0.965796	0.993645
OC–40%	0.997963	0.964356	0.995638
LAC–20%	0.997523	0.957360	0.997687
LAC–40%	0.997778	0.978825	0.993260
Maximum relative error	1.598%	3.142%	——

5.2. Weibull Probability Distribution Model (WPDM)

The decay model expression of aeolian sand concrete total failure energy U under freeze–thaw cycles was established using the Weibull probability distribution as follows:

$$U_n = U_0(1 - D_n) \quad (18)$$

where U_0 represents the total failure energy of concrete in the absence of freeze–thaw action; U_n denotes the total failure energy of concrete after n freeze–thaw cycles; and D_n is the damage variable after n times freeze–thaw.

Assume that f_n represents the probability density function following n freeze–thaw cycles.

$$f_n = \frac{b}{a}\left(\frac{n}{a}\right)^{b-1}\exp\left[-\left(\frac{n}{a}\right)^{b}\right] \tag{19}$$

where a is the shape parameter and b is the size parameter.

The failure probability distribution function is derived by integrating Equation (19).

$$F_n = 1 - \exp\left[-\left(\frac{n}{a}\right)^{b}\right] \tag{20}$$

The relationship between failure probability and the number of freeze–thaw cycles is shown in Equation (20). The freeze–thaw failure of aeolian sand concrete is the result of the long–term accumulation of freeze–thaw damage; thus, the damage variable and failure probability are simultaneously superimposed. After n times freeze–thaw cycles of aeolian sand concrete, D_n represents the damage degree and F_n represents failure probability. When the concrete reaches freeze–thaw failure, $D_n = F_n = 1$, the failure probability is equivalent to the damage degree:

$$D_n = 1 - \exp\left[-\left(\frac{n}{a}\right)^{b}\right] \tag{21}$$

5.3. Analysis of Reliability Results

In addition, Monte Carlo simulation (MCS) with 1 million sample points was used to evaluate the reliability of the series structure system, and the results are listed in Tables 6 and 7.

Table 7. Failure probability calculation results using different methods.

	Proposed Method	**WPDM**	**MCS**
OC–60%	0.997732	0.995572	0.998655
LAC–60%	0.985404	0.964223	0.996215
Maximum relative error	1.085%	3.211%	——

Similarly, according to the above method, the reliability and failure probability can be determined under 25, 50, …, and 175 freeze–thaw cycles; a custom neural network was constructed with reliability and failure probability as inputs and the number of freeze–thaw cycles as outputs. According to the empirical equation [29], the number of hidden layer elements was taken as the hidden layer $m = 5$ and activation function $f = e^{-x}$. After training 1000 steps, the relative dynamic modulus and mass loss rate under the same freeze–thaw cycle were taken as the x– and y–axis coordinates, and the fitting curve was drawn, as shown in Figure 13. The maximum relative error of the fitting results compared with the training output sample is listed in Table 8.

Table 8. Maximum relative error of fitting.

Category	**OC–20%**	**OC–40%**	**OC–60%**	**LAC–20%**	**LAC–40%**	**LAC–60%**
Maximum relative error	1.43×10^{-4}	4.29×10^{-6}	1.82×10^{-5}	2.80×10^{-4}	4.41×10^{-4}	1.11×10^{-6}

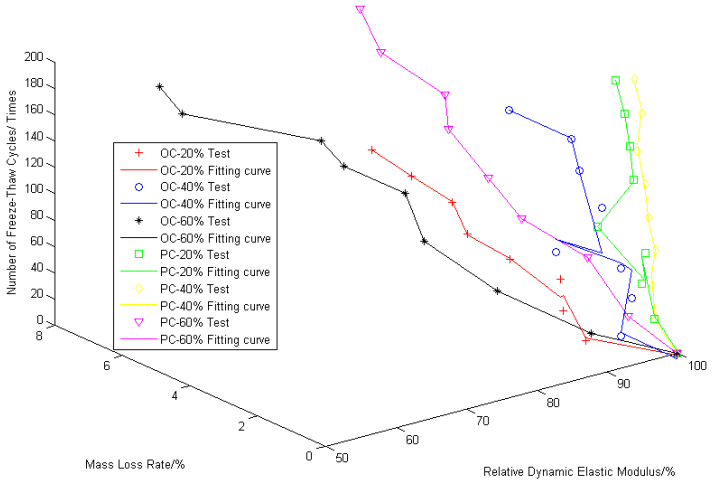

Figure 13. Fitting curve of eolian sand concrete using the custom neural network.

If either the relative dynamic elastic modulus loss or mass loss meets the failure standard, the material is considered to have failed. Following training of the custom neural network, the predicted input samples that have reached failure are taken as the input of the neural network, and the number of freeze–thaw cycles when failure is obtained, as shown in Table 9.

Table 9. Freeze–thaw cycle failure times of aeolian sand concrete.

Category	OC–20%	OC–40%	OC–60%	LAC–20%	LAC–40%	LAC–60%
Freeze–thaw cycle failure	258	302	162	343	378	127

From the reliability calculation results of different methods shown in Tables 6 and 7, it can be seen that with MCS as the exact solution, the calculation accuracy of the proposed method depicted in this paper is better than that of the WPDM, and the maximum relative error is less than 2%.

It can be seen from Table 8 that the fitting accuracy of the custom neural network model for the freeze–thaw cycle failure of aeolian sand concrete is higher. Among the various types of aeolian sand concrete, the highest relative error is 4.41×10^{-4}, with the remaining errors all falling below this value, with some found to be even as low as 1.0×10^{-6} orders of magnitude, demonstrating excellent calculation accuracy.

Based on the proposed method described in this paper, the reliability analysis model was obtained to accurately calculate the reliability of various types of aeolian sand concrete to accurately predict the number of freeze–thaw cycles of various types of aeolian sand concrete during failure.

As can be seen from Table 9, OC–60% and LAC–60% fail first, and the number of freeze–thaw cycles for these samples is 162 and 127, respectively, which is consistent with the test results. This result verifies the effectiveness of the custom neural network model. The freeze–thaw cycle durability of the aeolian sand concrete with equal replacement rates of 20% and 40% is evidently better than that of the aeolian sand concrete with 60% aeolian sand concrete, and the optimal ratio is the aeolian sand concrete with a replacement rate of 40%. The reliability of light aggregate concrete with aeolian sand replacement rates of 20% and 40% is slightly better than that of ordinary concrete with aeolian sand, with the best concrete being LAC–40%, and the number of freeze–thaw cycles reaching 378.

6. Conclusions

In this study, scanning electron microscopy (SEM) and X-ray diffraction (XRD) were employed to repeatedly assess the damage parameters of aeolian sand concrete structures, with their relative dynamic elastic modulus and mass loss rate under various freeze–thaw

cycles being ultimately determined. The edge statistical distribution of each damage parameter was determined using mathematical statistics. Considering the correlation between damage parameters, the reliability of aeolian sand concrete structures can be more accurately reflected. The Copula method was utilized to develop the joint probability density function for the damage parameters of concrete structures, and structural reliability was determined using a dual neural network approach. Using the above methods enabled the accurate prediction of freeze–thaw cycle failure times for aeolian sand concrete and the following conclusions can be drawn:

(1) In the reliability analysis of aeolian sand concrete freeze–thaw failure, the relative dynamic elastic modulus attenuation and mass loss rate reflect the law of specimens changing with changes in the number of freeze–thaw cycles. The relative dynamic elastic modulus decreases as the number of freeze–thaw cycles increases, with significant decreases observed in OC–20% and OC–60%. Additionally, the mass loss rate increases with the number of freeze–thaw cycles. The mass loss rate of OC–60% and LAC–60% increased significantly, and both exceeded the failure standard of 5%.

(2) The reliability analysis model proposed in this paper can effectively describe the deterioration trend in the frost resistance of aeolian sand concrete specimens. With MCS of 1 million sample points as the theoretical solution, the maximum relative error of WPDM reliability and failure probability calculation results is greater than 3% under 200 freeze–thaw cycles, and the maximum relative error of the proposed method is close to 1%, which reflects suitable calculation accuracy. Based on the test data, the proposed reliability analysis model can directly reflect the reliability of the test piece and its remaining life to provide relevant theoretical guidance and maintenance diagnosis for practical engineering.

(3) According to the prediction of the custom neural network model, the aeolian sand concrete with a replacement rate of 60% has the lowest number of freeze–thaw cycles, all less than 200, while the aeolian sand concrete with a replacement rate of 40% has the highest number of freeze–thaw cycles, all more than 300. Therefore, the optimal ratio is the aeolian sand concrete sample with a replacement rate of 40%. The reliability of lightweight aggregate concrete containing aeolian sand is slightly better than ordinary concrete containing aeolian sand under freeze–thaw cycles.

(4) The advantage of the method described in this paper is that the construction of the edge probability density function of damage parameters and the selection of the Copula function can be independently carried out, and a joint probability density function construction method based on the Copula function is proposed, which provides a new method for the accurate description of the correlation of damage parameters of aeolian sand concrete structures.

(5) In the present study, mass loss and relative dynamic elastic modulus were used as indicators to study the freeze–thaw cycle damage of aeolian sand concrete under different mix ratios, and the dual neural network method was used to model the performance degradation process of aeolian sand concrete for reliability analysis, which provides a theoretical basis for the effective utilization of aeolian sand and other low–quality natural resources. This, in turn, creates conditions for the extensive use of aeolian sand concrete in engineering practice.

Author Contributions: Conceptualization, Y.H. and H.X.; methodology, Y.H.; software, J.D.; validation, Y.H. and J.D.; formal analysis, Y.H.; data curation, H.X.; writing—original draft preparation, Y.H.; writing—review and editing, H.X.; funding acquisition, Y.H. All authors have read and agreed to the published version of the manuscript.

Funding: This work was supported by the Program for Improving the Scientific Research Ability of Youth Teachers of Inner Mongolia Agricultural University under Grant No. BR240101 and BR220115, Inner Mongolia Natural Science Foundation Project under Grant No. 2023LHMS01012 and 2023QN01006, Inner Mongolia Autonomous Region Higher Education Institutions Science Research Project under Grant No. NJZY23053, Inner Mongolia Autonomous Region Directly Affiliated Higher

Education Institutions Basic Science Research Fund Project under Grant No. NCYWT23027, Inner Mongolia Agricultural University High–Level Talent Introduction Research Project under Grant No. NDYB2018-42, Science and Technology Plan Project of Inner Mongolia Autonomous Region under Grant No. 2022YFHH0075.

Data Availability Statement: Data is contained within the article. The original contributions presented in the study are included in the article, further inquiries can be directed to the corresponding authors.

Conflicts of Interest: The authors declare no conflicts of interest.

References

1. Elipe, M.G.; López–Querol, S. Aeolian Sands: Characterization, Options of Improvement and Possible Employment in Construction–The State–of–The–Art. *Constr. Build. Mater.* **2014**, *73*, 728–739. [CrossRef]
2. Wu, J.; Shen, X.; Dong, W.; Hao, Y. Research Status of Engineering Application and Durability of Aeolian Sand Cement Based Concrete. *Bull. Chin. Ceram. Soc.* **2015**, *34*, 2845–2850.
3. Bai, J.; Zhao, Y.; Shi, J.; He, X. Damage Degradation Model of Aeolian Sand Concrete Under Freeze–Thaw Cycles Based on Macro–Microscopic Perspective. *Constr. Build. Mater.* **2022**, *327*, 126882. [CrossRef]
4. Zhou, M.; Dong, W. The Relationship between Pore Structure and Strength of Aeolian Sand Concrete under Low Temperature. *J. Build. Eng.* **2023**, *80*, 108067. [CrossRef]
5. Seif, E.-S.S.A. Assessing The Engineering Properties of Concrete Made with Fine Dune Sands: An Experimental Study. *Arab. J. Geosci.* **2011**, *6*, 857–863. [CrossRef]
6. Zhang, H.; Zheng, S.; Jing, P.; Yuan, C.; Li, Y. Influence of Pore Structure Characteristics on The Strength of Aeolian Sand Concrete. *Građevinar* **2024**, *76*, 35–45.
7. Zhu, J.; Liu, Q.; Han, F.; Zheng, S.; He, Y. Modified Damage Model of Aeolian Sand Self–Compacting Concrete. *J. Eng. Mech.* **2024**, *150*, 04024044. [CrossRef]
8. Jiang, J.; Wang, L.; Chu, H.; Wang, F.; Ju, S.; Gu, Y. Workability, Hydration, Microstructure, and Mechanical Properties of UHPC Produced with Aeolian Sand. *J. Sustain. Cem.–Based Mater.* **2022**, *11*, 215–226. [CrossRef]
9. Dong, W.; Shen, X.; Xue, H.; He, J.; Liu, Y. Research on The Freeze–Thaw Cyclic Test and Damage Model of Aeolian Sand Lightweight Aggregate Concrete. *Constr. Build. Mater.* **2016**, *123*, 792–799. [CrossRef]
10. Bai, J.; Xu, R.; Zhao, Y.; Shi, J. Flexural Fatigue Behavior and Damage Evolution Analysis of Aeolian Sand Concrete Under Freeze–Thaw Cycle. *Int. J. Fatigue* **2023**, *171*, 107583. [CrossRef]
11. Zhao, G.; He, Z.; Yang, H. Durability of Concrete under Freeze–Thaw Cycle and Carbonization. *Eng. J. Wuhan Univ. (Eng. Sci.)* **2013**, *46*, 604–609.
12. Jiang, N.; Liu, Y.; Deng, Y.; Yu, F. Reliability Assessment of Concrete under Chloride Penetration and Fatigue Loading Based on Copula Function. *J. Mater. Civ. Eng.* **2020**, *32*, 4020366. [CrossRef]
13. Lydia, M.; Nassim, K. Reliability Analysis and Comparative Study of Ordinary Concrete and High Performance Concrete Filled with Steel Tube under Axial Compression. *Int. J. Eng. Res. Afr.* **2022**, *61*, 245–261. [CrossRef]
14. Qiao, H.; Peng, K.; Chen, K.; Li, J.; Zhu, X. Reliability Analysis of Freeze–Thaw Failure of Ceramic Powder Recycled Concrete. *Mater. Rev.* **2020**, *34*, 10035–10040.
15. Lu, C.; Qiao, H.; Wei, Z.; Li, K.; Fu, Y. Mechanism of Accelerated Failure and Deterioration of Concrete in Saline Soil Area and Reliability Analysis Based on Wiener Process. *J. China Univ. Min. Technol.* **2021**, *50*, 265–272.
16. Qiao, H.; Peng, K.; Chen, K.; Li, J.; Guang, L. Analysis of Sulfate Resistance and Reliability of Recycled Ceramic Powder Concrete under Dry–wet Cycle Conditions. *J. Basic Sci. Eng.* **2021**, *29*, 752–760.
17. Lu, C.; Wei, Z.; Qiao, H.; Qiao, G.; Zhu, B. Reliability Analysis Method of Accelerated Life Test for Concrete in Saline Soil Area. *J. Cent. South Univ. (Sci. Technol.)* **2021**, *52*, 1017–1026.
18. Jiao, J.; Zhu, J. Reliability Analysis of Freeze–Thaw Failure of Recycled Concrete. *Bull. Chin. Ceram. Soc.* **2020**, *39*, 1145–1152.
19. Gasperlin, M.; Tusar, L.; Tusar, M.; Kristl, J.; Smid-Korbar, J. Lipophilic Semisolid Emulsion Systems: Viscoelastic Behaviour and Prediction of Physical Stability by Neural Network Modelling. *Int. J. Pharm.* **1998**, *168*, 243–254.
20. Xue, J.; Shao, J.F.; Burlion, N. Estimation of Constituent Properties of Concrete Materials with an Artificial Neural Network Based Method. *Cem. Concr. Res.* **2021**, *150*, 106614. [CrossRef]
21. Al-Haik, M.S.; Hussaini, M.Y.; Garmestani, H. Prediction of Nonlinear Viscoelastic Behavior of Polymeric Composites Using an Artificial Neural Network. *Int. J. Plast.* **2006**, *22*, 1367–1392. [CrossRef]
22. Khafajeh, R.; Shamsaei, M.; Tehrani, H.G.; Easa, S.M. Proposing Load Transfer Efficiency as Criterion for Repairing Longitudinal and Transverse Cracks of Asphalt Pavements. *J. Transp. Eng. Part B Pavements* **2021**, *147*, 06021002. [CrossRef]
23. Li, Y.; Zhang, H.; Chen, S.; Wang, H.; Liu, G. Multi–Scale Study on The Durability Degradation Mechanism of Aeolian Sand Concrete under Freeze–Thaw Conditions. *Constr. Build. Mater.* **2022**, *340*, 127433. [CrossRef]
24. *GB/T 50081-2019*; Ministry of Construction of the People's Republic of China. Standard for Test Methods of Concrete Physical and Mechanical Properties. China Architecture and Building Press: Beijing, China, 2019; pp. 5–69.

25. *GB/T 50082-2009*; Ministry of Construction of the People's Republic of China. Standard for Test Methods of Long–Term Performance and Durability of Ordinary Concrete. China Architecture and Building Press: Beijing, China, 2009; pp. 6–27.
26. Chen, R.; Qiao, P. Characterization of Concrete Micro–Durability Based on Nanoindentation Test. *Chin. Q. Mech.* **2015**, *36*, 88–94.
27. Nelsen, R.B. *An Introduction to Copulas*, 2nd ed.; Springer: New York, NY, USA, 2006; pp. 51–108.
28. Li, H.B.; He, Y.; Nie, X.B. Structural Reliability Calculation Method Based on the Dual Neural Network and Direct Integration Method. *Neural Comput. Appl.* **2018**, *29*, 425–433. [CrossRef]
29. He, Y.; Li, H.B.; Du, J. Fitting Methods Based on Custom Neural Network for Relaxation Modulus of Viscoelastic Materials. *Int. J. Perform. Eng.* **2019**, *15*, 107–115. [CrossRef]